

Identifying suboxide grains at the metal-oxide interface of a corroded Zr-1.0%Nb alloy using (S)TEM, transmission-EBSD and EELS

Jing Hu¹, Alistair Garner², Na Ni³, Ali Gholinia², Rebecca Nicholls¹, Sergio Lozano-Perez¹, Philipp Frankel², Michael Preuss², Chris Grovenor¹

1. Department of Materials, Oxford University, Parks Road, Oxford, UK

2. Materials Performance Centre, School of Materials, University of Manchester, Manchester, UK

3. Department of Materials, Imperial College London , Royal School of Mines, London, UK

Email: jing.hu@materials.ox.ac.uk

Phone: + 44 (0)7583260056

Highlights:

1. Combination of (S)TEM, transmission-EBSD and EELS allows precise analysis of suboxide grains at the metal-oxide interface of corroded Zr-1.0%Nb alloys.
2. EELS analysis confirms the existence of stoichiometric ZrO phase at the metal-oxide interface.
3. Transmission-EBSD confirms that these grains have the theoretically predicted hexagonal ZrO crystal structure and allows for mapping of the grain morphology across a large area of the interface.

Abstract

Here we report a methodology combining TEM, STEM, Transmission-EBSD and EELS to analyse the structural and chemical properties of the metal-oxide interface of

corroded Zr alloys in unprecedented detail. TEM, STEM and diffraction results revealed the complexity of the distribution of suboxide grains at the metal-oxide interface. EELS provided accurate quantitative analysis of the oxygen concentration across the interface, identifying the existence of local regions of stoichiometric ZrO with varying thickness. Transmission-EBSD confirmed that the suboxide grains can be indexed with the hexagonal ZrO structure predicted with *ab initio* by Nicholls et.al¹. The t-EBSD analysis has also allowed for the mapping of a relatively large region of the metal-oxide interface, revealing the location and size distribution of the suboxide grains.

Keywords

Zirconium alloys; (S)TEM; Transmission-EBSD; EELS; Suboxide; Oxidation mechanism

1. Introduction

Zirconium alloys are used extensively as cladding materials in modern light water reactors. The purpose of the cladding material is to separate the uranium dioxide (UO₂) fuel rods and the coolant water in order to prevent the escape of fission products whilst maintaining heat transfer to the coolant. The widespread use of these alloys is mainly due to their low thermal neutron capture cross section and good corrosion performance in the aggressive reactor environment²⁻⁴. With increasing demand for high burn-up in modern nuclear reactors, environmental degradation of these alloys is now the life-limiting factor for fuel assemblies².

The general waterside corrosion kinetics of zirconium alloys has two stages: the first is an initial pre-transition period of slow parabolic or cubic corrosion which can be fitted

using the power law equation, $\Delta W = Kt^n$ (W is the weight gain in mg/dm^2 , K depends on both alloying elements and reactor temperature, and t is the oxidation time in days). At a critical thickness ($\sim 2\mu\text{m}$), the previously protective oxide begins to break down and there is an abrupt increase in corrosion rate, often termed the *transition*. The protective oxide then builds up again and post-transition corrosion is composed of several cycles that mimic pre-transition corrosion until a period of rapid linear growth eventually develops^{5,6}. Post-transition corrosion generally follows an expression of form $\Delta W = Kt + C$ (where C is the initial weight gain). The Zr-1.0%Nb alloy used in this investigation has been shown to exhibit a delayed transition when compared to other Nb-containing alloys⁷.

During corrosion, an adherent oxide film is formed by the dissociation of water molecules at the outer surface of the oxide. Oxygen ions then diffuse inwards, forming an oxide that grows into the metal. The metal-oxide interface is thus of particular interest as it is the location of the oxidation reaction and is expected to play an important role in controlling the corrosion behaviour. Yilmazbayhan et.al⁸ used Transmission Electron Microscopy (TEM) to show there are 100–150 nm wide rectangular blocky suboxide grains near the metal-oxide interface on a Zr-2.5%Nb alloy. Abolhassani et.al⁹ also identified a substoichiometric phase with 40–60 at.% oxygen at the interface of irradiated Zr-2.5%Nb using Energy Dispersive X-ray Spectroscopy (EDS). Ni and Hudson¹⁰ used Electron Energy Loss Spectroscopy (EELS) and Atom Probe Tomography (APT) to study oxidized ZIRLO™ and Zircaloy-4 alloys, and found a suboxide layer with composition of ZrO at the metal-oxide interface in pre-transition samples which disappears after transition. Nishino et. al¹¹ used Auger Electron Spectroscopy (AES) and X-ray Photoelectron Spectroscopy (XPS) to study the initial

oxidation of Zircaloy-2 at room temperature, and identified Zr_2O , ZrO and Zr_2O_3 suboxide phases on the oxidized surfaces. The equilibrium ZrO binary phase diagram contains no stable phases with these stoichiometries, but Density Functional Theory (DFT) modelling performed by Puchala et al¹² and Nicholls et. al¹ predicts a stable ZrO suboxide phase with a hexagonal structure as well as other stoichiometric phases not in the ZrO binary phase diagram, including Zr_2O .

It has previously been demonstrated that the micro-chemistry and crystallography at this metal-oxide interface is extremely complex and localised¹⁰. The techniques used to examine the metal-oxide interface are usually focused on a very small region and so it is difficult to correlate the local appearance of suboxide phases to the overall corrosion performance of different alloys. In this paper we present a methodology combining TEM, STEM, t-EBSD and EELS analysis to characterise the chemistry and crystallography of suboxide phases at the metal-oxide interface. T-EBSD also allows for characterisation of a relatively large suboxide region, giving a more general view of what is happening at this particular stage of the oxidation process.

2. Materials and Methods

The sample used for this investigation was prepared from a WestinghouseTM developmental alloy with composition of $\text{Zr-0.9Nb-0.01Sn-0.08Fe}$ (wt%) in the recrystallized condition. The sample was oxidized in an autoclave at EDF Energy under simulated Pressurized Water Reactor (PWR) water conditions at 360°C for 360 days, and shows no sign of accelerated oxidation rate and so is considered to be in the pre-transition stage of the corrosion cycle⁷.

A TEM sample was prepared by *in-situ* lift out method on an FEI FIB 200 using milling currents of 7000-100pA at 30kV, and further thinned down to a thickness below 100nm in a Zeiss Nvision 50 dual beam FIB using a beam current of 150pA at 30kV and then 250pA at 5kV to create a homogeneous and electron-transparent sample for TEM, STEM and t-EBSD analysis. The sample was further thinned down to ~70nm using the low-voltage conditions for final EELS analysis on selected regions of interest.

TEM and STEM analysis were performed on a JEOL 2100 LaB6 microscope operated at 200kV. EELS analysis was performed on an FEI Titan microscope operated at 300kV and equipped with a Gatan image filter. The convergence half-angle α was 10mrad and collection half-angle β was 12mrad with an energy dispersion of 0.5eV per channel and a step size of 10nm. T-EBSD¹³ was performed on an FEI Magellan FEG-SEM XHR 400L at 30kV with a probe current of 1.6nA. The step size for t-EBSD was 15nm, with an acquisition speed of 33.5Hz, the total map time was 1 hour 11 minutes. In order to achieve optimal spatial resolution, the EBSD measurements were performed in transmission geometry. The sample was tilted at 20° away from the EBSD detector with a working distance of 2mm. The Kikuchi patterns were indexed using the AZtec software suite developed by Oxford Instruments. The EBSD measurements in transmission geometry allowed an optimal spatial resolution of ~10nm, necessary for the study of the extremely fine microstructure at the metal-oxide interface¹⁴.

3. Experimental results

3.1. (Scanning) Transmission Electron Microscopy

Figure 1(a) shows a bright field (BF) image of the TEM sample. Below the Pt layer, which is used to protect the sample during FIB milling, a ZrO_2 layer of thickness $2.8\mu\text{m}$ can clearly be seen. The oxide layer consists of equiaxed grains on the outer surface and columnar grains towards the metal-oxide interface. There are some lateral cracks visible throughout the oxide, the largest of which are located near the metal-oxide interface. The high annular dark-field (HAADF) STEM image of the same area in Figure 1(b) shows metallic second phase particles embedded in the oxide with voids above them. Below the metal-oxide interface, large zirconium metal grains are visible in both images, with embedded metallic second phase particles. A similar general microstructure has been seen in oxidized Zr alloys by many previous authors^{8,10}. The insets in Figure 1(a) and Figure 1(b) are higher magnification TEM bright field and STEM HAADF images of the region chosen for EELS analysis. In all these images, there is a slight contrast change at the metal-oxide interface but it is difficult to distinguish if there are phases other than ZrO_2 and metallic Zr in this region.

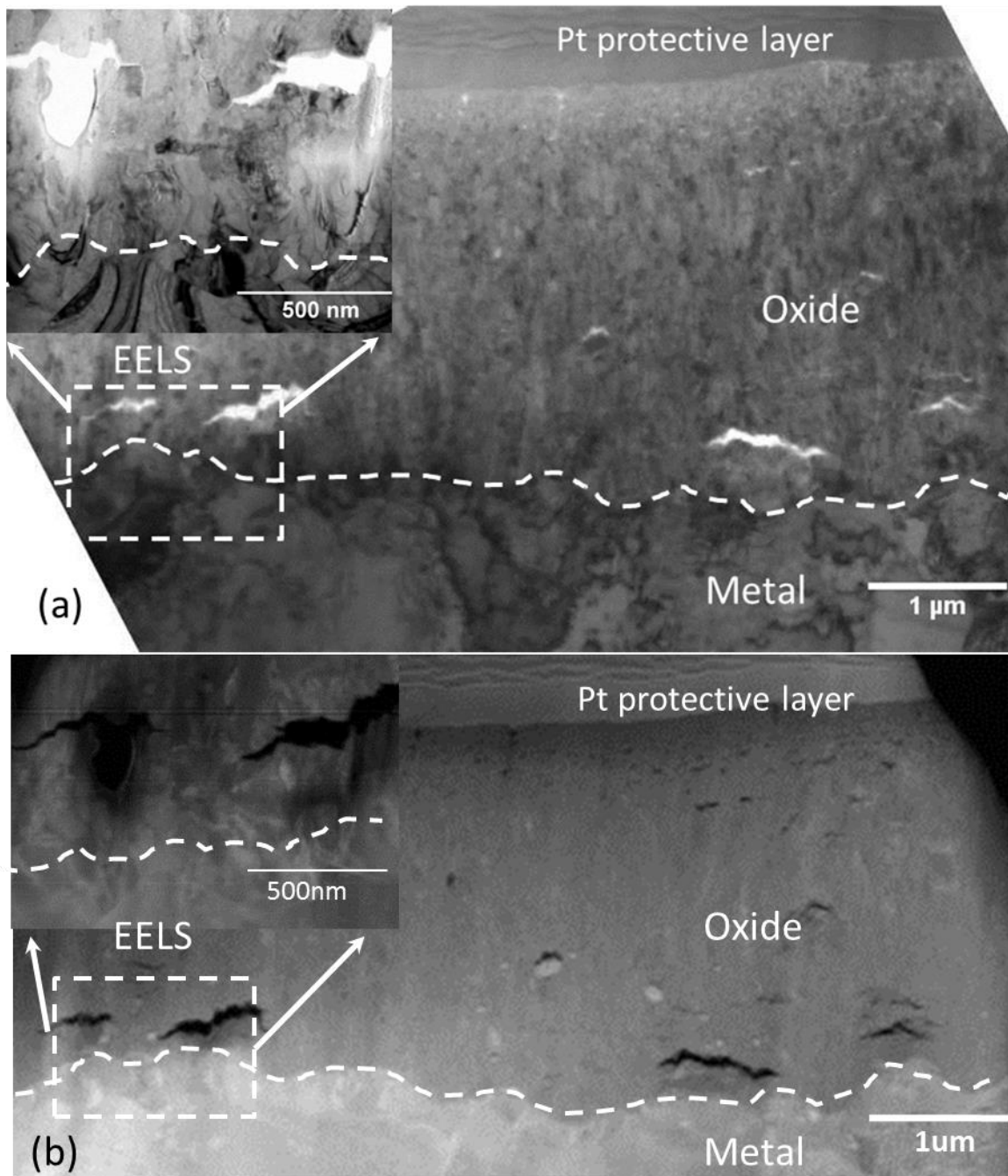


Figure 1(a): TEM Bright field image of the TEM sample. Figure 1(b): HAADF-STEM image of the TEM sample. The area used for EELS analysis is highlighted. The inset shows higher magnification images of this same area after further FIB thinning (which has created the hole under the left hand crack)

Convergent beam electron diffraction (CBED) patterns were acquired from a region close to the metal-oxide interface just between the two cracks shown in the higher

magnification TEM bright field image in Figure 2(a). A suboxide grain which is strongly diffracting is highlighted by the arrows. A STEM dark field image of the suboxide grain area is shown in Figure 2(b); the Z-contrast helps to identify the suboxide as a region of intermediate contrast between the brighter metal substrate and the darker stoichiometric ZrO_2 highlighted by arrows in the figure. The area where the CBED pattern was taken is also highlighted. A typical diffraction pattern is shown in Figure 2(c) and can be indexed as matching with the $[32\bar{4}]$ zone axis of the hexagonal ZrO phase with P-62m symmetry and lattice parameters $a=5.31 \text{ \AA}$ and $c=3.20 \text{ \AA}$ predicted by Nicholls et al¹.

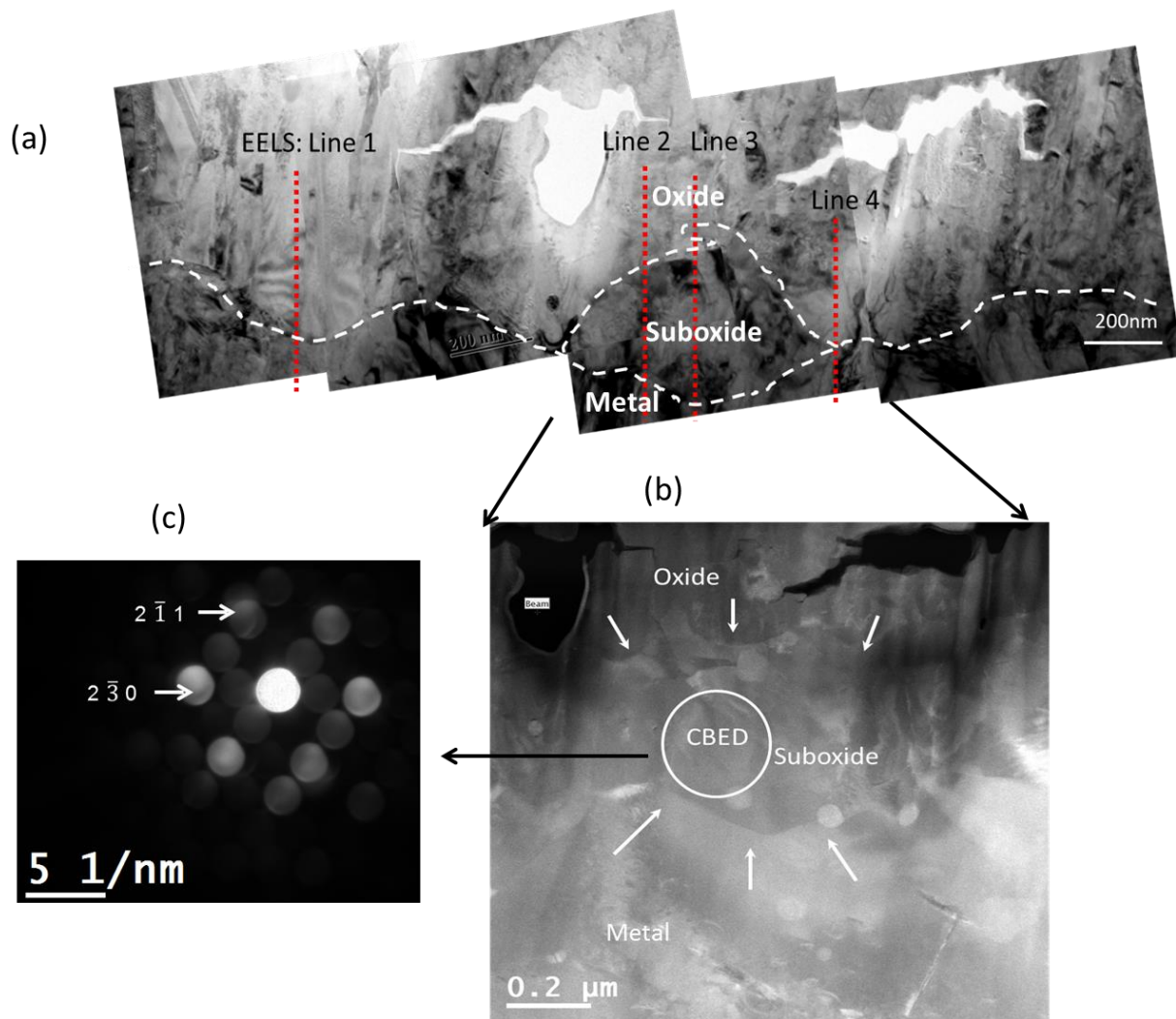


Figure 2: (a) High magnification TEM bright field image of the area near the metal-oxide interface, which was chosen for EELS analysis. The suboxide grain, which was in a strongly diffracting condition, is highlighted using arrows. (b) STEM dark field image of the suboxide grain area, with the area where CBED pattern was taken highlighted. (c) CBED pattern of the suboxide grain which matched with the predicted hexagonal ZrO phase with $P-62m$ symmetry and lattice parameters $a=5.31 \text{ \AA}$ and $c=3.20 \text{ \AA}$.

3.2. Transmission- EBSD

The band contrast image from the t-EBSD analysis shown in Figure 3(a) highlights the typical oxide microstructure, with small equiaxed grains towards the outer surface and large, elongated monoclinic grains towards the interface, oriented parallel with the oxide growth direction^{8,10}. At the interface, blocky grains are clearly visible, which correspond well with the appearance of suboxide grains described by other authors⁸. Some of the grains at the interface are identified as the hexagonal ZrO phase with P-62m symmetry and lattice parameters $a=5.31 \text{ \AA}$ and $c=3.20 \text{ \AA}$ ¹, while other grains match Zr metal with P 63/m symmetry and lattice parameters $a=3.23 \text{ \AA}$ and $c=5.14 \text{ \AA}$ ¹⁵. The patterns were also checked against the orthorhombic ZrO phase predicted by Nicholls et al.¹, however there was no match in any of the interfacial grains. To show how we verify the structure of these suboxide grains, the Kikuchi patterns (EBSPs) from this region were matched using the AZtec software suite with the hexagonal ZrO phase predicted by Nicholls et al.¹. Examples of matched EBSPs acquired from the suboxide region are shown in

Figure 4, with the software providing consistent matching with a mean angular deviation of generally $\sim 0.5^\circ$. The phase map for the entire region is shown in

Figure 3(b). This map shows, as expected, that the majority of the oxide is composed of columnar monoclinic ZrO₂ grains, and small tetragonal ZrO₂ grains are also visible throughout the oxide. The tetragonal phase fraction is $\sim 1\%$, which is below the fraction of $\sim 3\%$ measured on this alloy at a similar exposure time using synchrotron X-Ray Diffraction (XRD)¹⁶. The average grain size for the tetragonal ZrO₂ grains is about 20nm. This is thought to be due to the transformation of the stress-stabilized tetragonal grains to the equilibrium monoclinic phase during preparation of the FIB sample, also the fact that the majority of the remaining tetragonal grains are below the resolution limit

of t-EBSD. At the metal-oxide interface, there is a clear layer composed of hexagonal ZrO grains. The ZrO grains are generally equiaxed and vary in size from ~50-300nm. The orientation map in Figure 3(c) indicates that most (but not all) of the suboxide grains inherit the orientation of the metal grain on which they form. Several examples of this epitaxial growth of suboxide are circled.

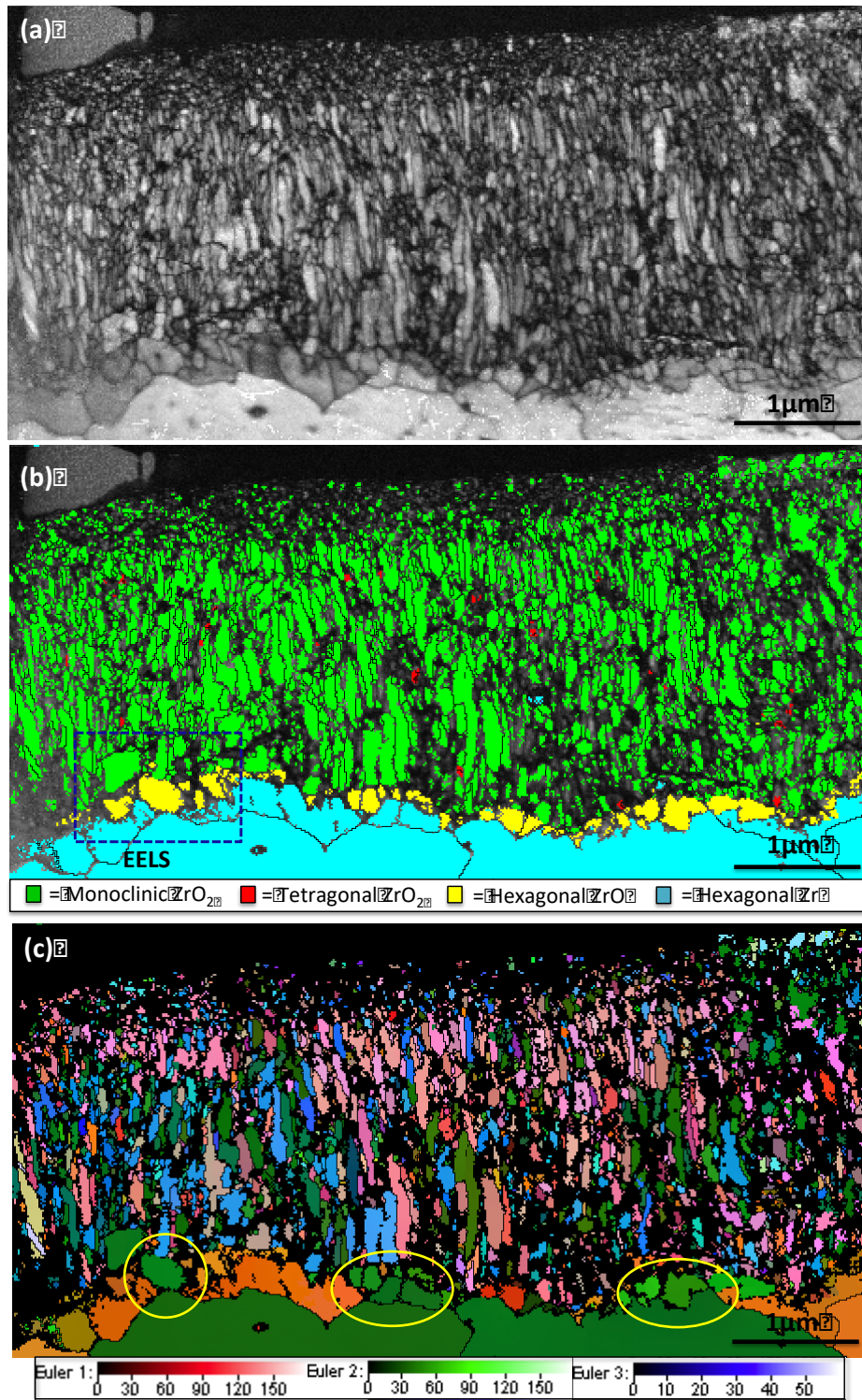


Figure 3: (a) Band contrast map, (b) Phase map and (c) Orientation map from *t*-EBSD analysis of the TEM sample (grain boundaries $>10^\circ$ are highlighted). The area for EELS and CBED analysis is also highlighted in (b). Circles in (c) show examples of epitaxial growth of the ZrO suboxide on the underlying Zr grains.

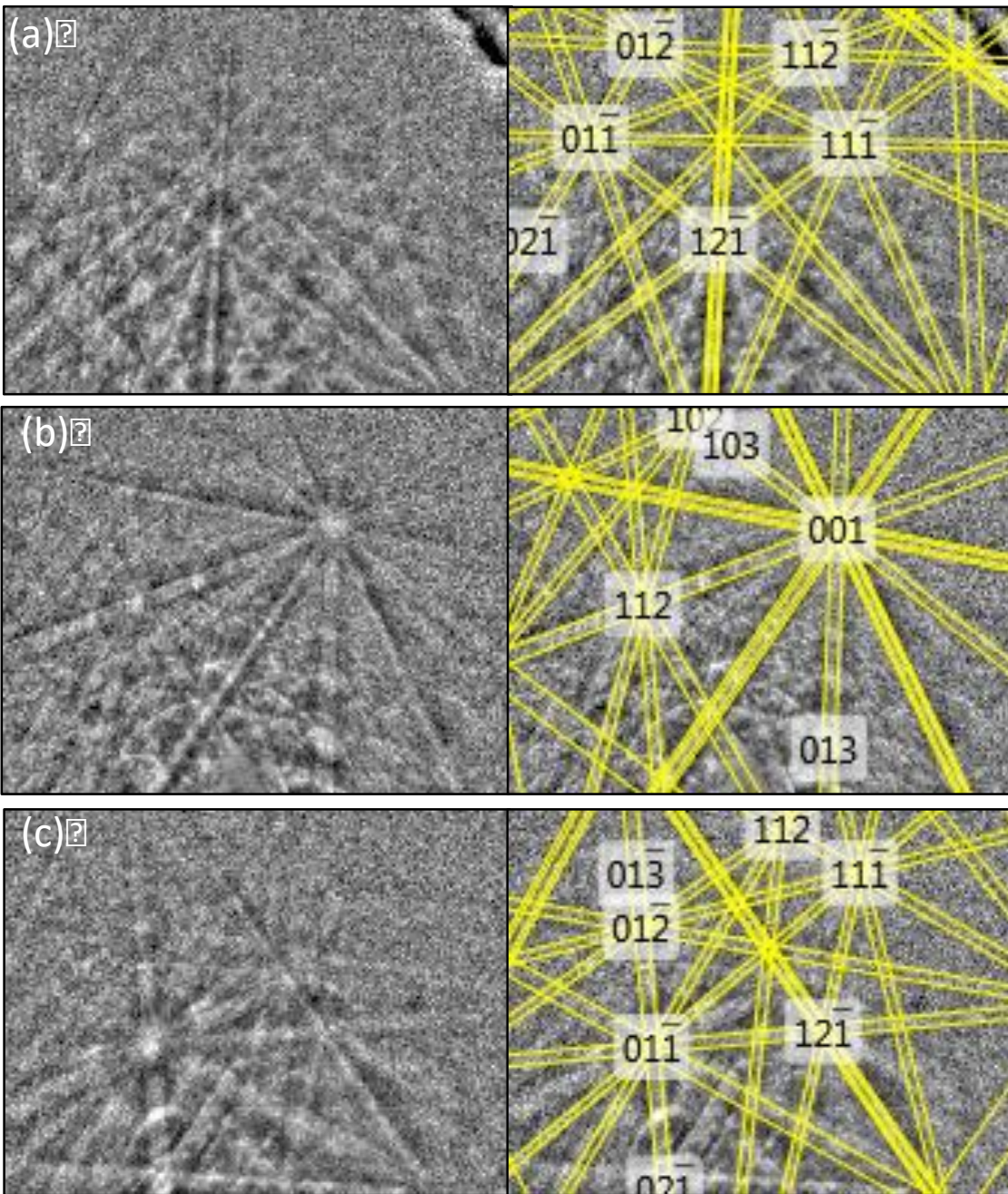


Figure 4: Selected electron backscattered patterns (EBSPs) from the suboxide region of the TEM sample and corresponding solutions using AZtec software and ZrO hexagonal phase (a) Mean angular deviation (MAD) = 0.45° number of matched bands = 7, (b) MAD = 0.59° number of bands = 7, (c) MAD = 0.57° number of bands = 8.

3.3 EELS analysis

Several EELS line profiles were performed in the region highlighted in Figures 1, 2 and 3, and the exact positions of the profiles are shown on the detail of the t-EBSD image in Figure 5(a) and the HAADF image in Figure 5(b). The sample thickness after final thinning for EELS was estimated to be around 70 nm. The oxygen concentration was calibrated by using the starting point of the line in the ZrO_2 region using the method described by Ni et.al¹⁷. In this region, both t-EBSD and CBED have confirmed the existence of hexagonal ZrO. The HAADF image also shows grain structures with different contrasts at the interface, and several second phase particles.

Four EELS profiles were taken in total from this region, with all four detecting some regions with ZrO stoichiometry of thicknesses varying from 13nm to 326nm (Figure 6). The difference in thickness of the ZrO suboxide regions, even over such a small area, demonstrates the extremely heterogeneous nature of the suboxide, as has been commented on in previous work¹⁷. In addition, in the third profile a layer with a Zr:O ratio of 3:2 is detected. This may be a result of an inclined interface running through the sample thickness, therefore there is a contribution from overlapping Zr and ZrO grains. It has previously been shown that the t-EBSD patterns will be created preferentially from the exiting surface of the TEM sample¹⁸, and so it is likely that in this area there is metallic Zr on the front side of the sample and ZrO on the back surface.

We can be confident of the accuracy of these compositional measurements because we measure the ZrO_2 stoichiometry on the oxide side of all the scans. On the metal side of the interface there is a gradient of oxygen into the metal which also seems to vary over the small area analysed here, also in agreement with previous observations¹⁰. On line profiles 2 and 3, there seems to be another plateau region of around 100nm thickness

after the suboxide region with an oxygen content of 25 at% (Zr_3O), which suggests that the Zr metal here is saturated with oxygen. In all four line scans, the oxygen content drops to a value close to zero deeper into the metal, indicating that the final sample cleaning has successfully removed most of the surface oxide.

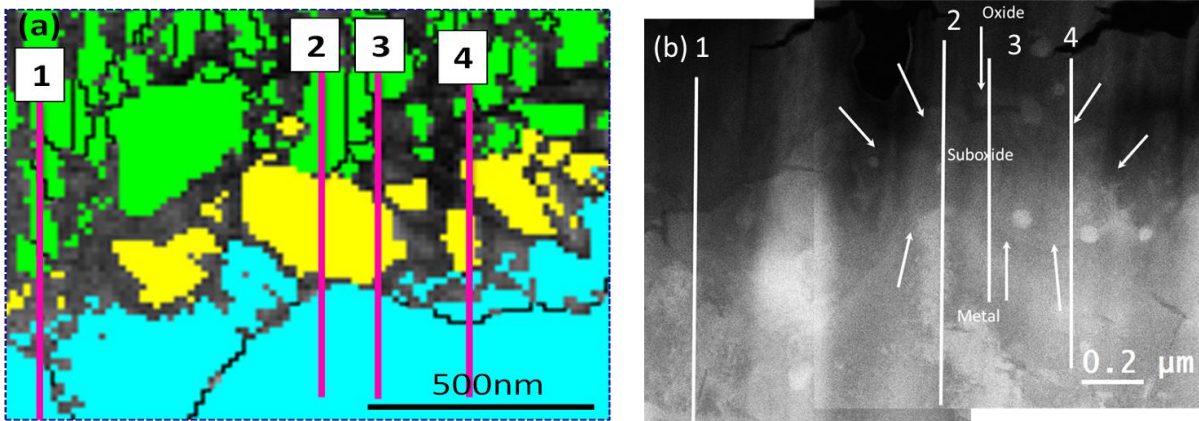


Figure 5. Positions of EELS line scans from the suboxide region relative to (a) the t-EBSD map. (b) the HAADF image. All profiles started from the oxide towards metal.

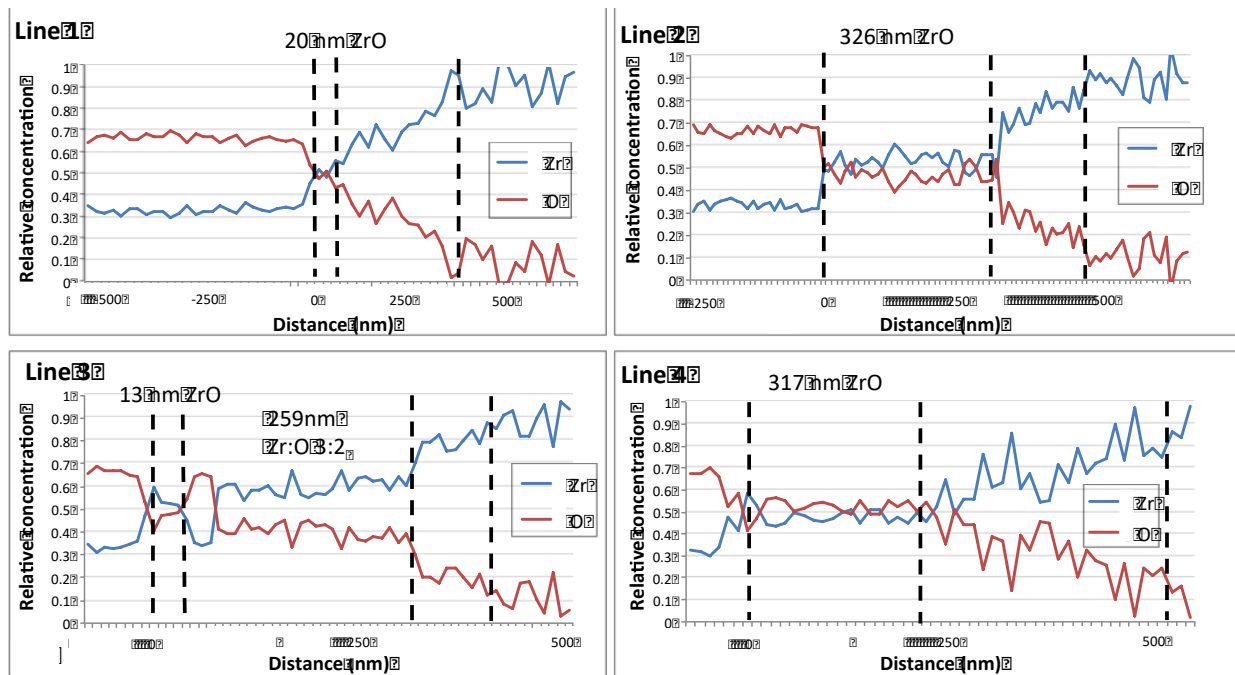


Figure 6: Positions of EELS line scans from the suboxide region relative to the HAADF image and *t*-EBSD map: (a) 20 nm ZrO₂, (b) 326 nm ZrO₂, (c) 13 nm ZrO₂+259 nm Zr₃O₂, (d) 317 nm ZrO₂.

4. Discussion

TEM images, as shown in Figures 1(a) and 2(a), can be used to highlight the microstructure of the oxide and the metal oxide interface, for instance the columnar ZrO₂ grain structure and the metal can clearly be distinguished. However, diffraction contrast imaging of the suboxide grains does not help us understand their chemistry. STEM HAADF images like those in Figures 1(b) and 5(b) are more useful due to the strong atomic number contrast¹⁹, so that the weight difference from different oxygen concentrations can easily be visualised. For instance, a suboxide region of different contrast at the metal-oxide interface can readily be seen in Figure 5(b).

The t-EBSD maps of the entire FIB sample are shown in Figure 3. Due to overlapping patterns at oxide grain boundaries, the oxide microstructure is highlighted in a way that is not possible with conventional TEM imaging. In the band contrast image, blocky grains are also visible at the metal oxide interface, and these grains are indexed with high confidence as the hexagonal ZrO phase predicted by DFT modeling¹, as shown in the phase map in Figure 3(b). The matched Kikuchi patterns in Figure 4 confirm that this modelled phase provides a good fit for this structure at the interface. In the region chosen for EELS analysis, there is a ZrO grain of diameter ~300nm, as well as smaller suboxide grains on either side. This map also shows the variation of thickness of the suboxide region along the metal-oxide interface. Although it appears that the ZrO layer is not continuous from the t-EBSD map, this could be due to the limited resolution of the technique (~10 nm) since all of the EELS line profiles show at least a very thin ZrO layer at the interface. More EELS profiles would be required to confirm this.

Because we can precisely identify the positions of the EELS line profiles on the HADDF and t-EBSD images, we can discuss how results from the different techniques compare on this small region of the interface. EELS profile 1 shows a relatively small ZrO region, which agrees well with the t-EBSD map at this location. The second EELS profile is taken across the centre of the large (~300 nm) diameter suboxide grain identified by t-EBSD as hexagonal ZrO and shows a clear 1:1 ZrO stoichiometry across the entire grain. The third profile, which is apparently taken across the edge of the same grain, appears to show a slightly different stoichiometry with a Zr:O ratio of 3:2. It shows a small ~13nm region of ZrO, which may coincide with the small oxide grain identified above the right hand side of the large grain in the t-EBSD image. As previously mentioned, it is possible that this increase in Zr ratio is caused by signal from an

overlapping Zr grain, due to the reduced ZrO thickness at the edge of the suboxide grain. The fourth EELS profile again shows the ZrO stoichiometry over a distance of ~300 nm at the interface. Comparison with the t-EBSD phase map suggests that the profile goes across two suboxide grains with the same hexagonal ZrO crystal structure. It is also important to note that the suboxide structure visible in the HAADF image in Figure 5(b) correlates well with the t-EBSD of this region in Figure 5(a).

Another interesting outcome of this work is the variation in the oxygen concentration gradient into the metal after the interface region. A comparison of EELS profiles 2 and 4 (Figure 6.) shows that in two regions that show a similar thickness of ZrO, the oxygen concentration gradients into the metal are quite different. The oxygen concentration along line profile 2 reduces to below 10% over a distance of ~100 nm, whereas along profile 4 has still not reached this level over ~300 nm. It can be seen from Figure 3 that beyond the suboxide grain, profile 2 enters a single ZrO₂ grain, whereas profile 4 enters a region of smaller ZrO₂ grains with a high level of non-indexed points. It is therefore possible that there are overlapping grains in this region causing different contributions to the Zr:O ratio along profile 4. It has previously been shown that the presence of the suboxide is correlated with corrosion rate and disappears after transition due to the increased local corrosion rate¹⁰. As mentioned previously, this sample appears to not have undergone the kinetic transition and so is in the pre-transition period of slow oxide growth, adding further evidence to the concept that the presence of the suboxide can be correlated with slow oxide growth. We note here that the transition could have occurred locally at some regions of the metal-oxide interface, even prior to the global increase in corrosion rate.

Comparing with data from other Zr alloys, it appears that this sample (Zr-0.9Nb-0.01Sn-0.08Fe) has a thicker suboxide layer than faster corroding alloys such as ZIRLO™. EELS data shows that pre-transition ZIRLO samples contain a 50nm ZrO layer which is thinner than is observed here¹⁷. Care must be taken when comparing these results as these observations clearly show a significant variation in suboxide thickness along even short lengths of the interface, but these results suggest that good oxidation resistance seems to be related to a thicker suboxide layer. At this point it is unclear whether this contributes to or is a result of the slower oxidation kinetics.

5. Conclusions

Here we report a methodology combining TEM, STEM, EELS analysis and t-EBSD to study suboxide phases at the metal-oxide interface of corroded Zr alloys. The appearance of the suboxide phase is shown to be localised and varied in distribution and composition, which makes it difficult to visualise in TEM imaging and therefore to acquire diffraction patterns to identify possible phases. T-EBSD gives an easier and more accurate way to match the candidate phases over a larger area and clearly reveals a suboxide layer at the metal-oxide interface. This suboxide is made up of approximately equiaxed grains of varying sizes, and it is clear that they do not form a uniform layer at the interface. EELS analysis allows for quantitative analysis of the oxygen concentration across the interface and reveals the presence of stoichiometric ZrO.

This work has shown that it is necessary for the suboxide region to be examined with a number of complementary techniques to ensure accurate characterisation of the complex microstructure. We have demonstrated that a number of techniques can be

applied to exactly the same volume of material if the original TEM specimen is of the appropriate quality and robustness. We believe that combining the techniques outlined here can be a powerful methodology used to characterise both the interfacial chemistry and crystallography of a wide range of engineering alloys where a complex nano-structure, often containing non-equilibrium phases stabilised by stress or other local parameters, may be difficult to study using a single technique.

Acknowledgements:

This project is part of the MUZIC-2 collaboration studying oxidation and hydrogen pickup in Zr alloys. The authors gratefully acknowledge support from EDF Energy, Westinghouse and Rolls Royce. Also, Jing Hu is supported by the China Scholarship Council.

References

1. Nicholls, R. J. *et al.* Crystal Structure of the ZrO Phase at Zirconium/Zirconium Oxide Interfaces. *Adv. Eng. Mater.* (2014). at <<http://doi.wiley.com/10.1002/adem.201400133>>
2. Pickman, D. O. Zirconium Alloy Performance in Light Water Reactors: A Review of UK and Scandanavian Experience. in *10th Int. Symp. Zircon. Nucl. Ind.* 19–32 (1994).
3. Cox, B. The Oxidation and Corrosion of Zirconium and its Alloys V: Mechanism of Oxide Film Growth and Breakdown on Zirconium and Zircaloy-2. *J. Electrochem. Soc.* **108**, 24–30 (1961).
4. Cox, B., Kritsky, V., Lemaignan, C. & Polley, V. Waterside corrosion of zirconium alloys in nuclear power plants. *IAEA TECDOC 684* (1998).
5. Hillner, E. Corrosion of zirconium based alloys. Zirconium in the Nuclear Industry: Third International Symposium, ASTM STP 633, American Society for Testing Materials. p. 211–23 (1977).

6. Garzarolli, F., Cox, B. & Rudling, P. *Corrosion and hydriding*. ANT International Report (2012).
7. Wei, J. *et al.* Autoclave study of zirconium alloys with and without hydride rim. *Corros. Eng. Sci. Technol.* **47**, 516–528 (2012).
8. Yilmazbayhan, A., Breval, E., Motta, A. T. & Comstock, R. J. Transmission electron microscopy examination of oxide layers formed on Zr alloys. *J. Nucl. Mater.* **349**, 265–281 (2006).
9. Abolhassani, S., Bart, G. & Jakob, a. Examination of the chemical composition of irradiated zirconium based fuel claddings at the metal/oxide interface by TEM. *J. Nucl. Mater.* **399**, 1–12 (2010).
10. Ni, N. *et al.* How the crystallography and nanoscale chemistry of the metal/oxide interface develops during the aqueous oxidation of zirconium cladding alloys. *Acta Mater.* **60**, 7132–7149 (2012).
11. Nishino, Y., Krauss, A., Lin, Y. & Gruen, D. Initial oxidation of zirconium and Zircaloy-2 with oxygen and water vapor at room temperature. *J. Nucl. Mater.* **228**, 346–353 (1996).
12. Puchala, B. & Van der Ven, a. Thermodynamics of the Zr-O system from first-principles calculations. *Phys. Rev. B* **88**, 094108 (2013).
13. Trimby, P. W. Orientation mapping of nanostructured materials using transmission Kikuchi diffraction in the scanning electron microscope. *Ultramicroscopy* **120**, 16–24 (2012).
14. Garner, a. *et al.* The microstructure and microtexture of zirconium oxide films studied by transmission electron backscatter diffraction and automated crystal orientation mapping with transmission electron microscopy. *Acta Mater.* **80**, 159–171 (2014).
15. Hull, A. The crystal structure of titanium, zirconium, cerium, thorium and osmium. *Phys. Rev.* **18**, 88–89 (1921).
16. Wei, J. *et al.* The effect of Sn on autoclave corrosion performance and corrosion mechanisms in Zr–Sn–Nb alloys. *Acta Mater.* **61**, 4200–4214 (2013).
17. Ni, N., Lozano-Perez, S., Sykes, J. & Grovenor, C. Quantitative EELS analysis of zirconium alloy metal/oxide interfaces. *Ultramicroscopy* **111**, 123–30 (2011).
18. Suzuki, S. Features of Transmission EBSD and its Application. *Jom* **65**, 1254–1263 (2013).
19. S. J. Pennycook, D. E. Jesson, A. J. M. and P. D. N. High angle dark field STEM for advanced materials. *J. Electron Microsc. Tech.* 36–43 (1996).

